From Grid to Cloud: Understanding the Impact of Grid Size on Simulated Anvil Clouds and Atmospheric Profiles

Zeyuan Hu[1], Nadir Jeevanjee[2], Zhiming Kuang[1,3]

[1]Department of Earth and Planetary Sciences, Harvard University, Cambridge, MA, USA
[2]Geophysical Fluid Dynamics Laboratory, Princeton, NJ, USA
[3]John A. Paulson School of Engineering and Applied Sciences, Harvard University, Cambridge, MA, USA

Key Points:

- We found a resolution dependence of anvil cloud fraction and updraft mass flux in simulations mostly due to the change of cloud-air mixing.
- We derived a self-consistent solution for a zero-buoyancy plume model as a simple tool to understand steady-state tropical atmosphere.
- We observed a convergence in atmospheric profiles, including anvil cloud fraction, at a grid resolution of approximately 100m.

Corresponding author: Zeyuan Hu, zeyuan_hu@fas.harvard.edu

Abstract

In this study, we explore the relationship between anvil cloud fraction and horizontal model resolution in small domain radiative-convective equilibrium (RCE) simulations, building on the findings of Jeevanjee and Zhou (2022). Using the System of Atmosphere Modeling (SAM) model, we find that finer resolutions yield higher anvil cloud fractions due to larger convective updrafts mass flux and increased mass detrainment at anvil levels. Employing two different microphysics schemes, we illustrate that finer resolution can enhance mass flux through either stronger cloud evaporation or weaker upper-troposphere stability, as the consequence of enhanced horizontal mixing. Moreover, we refine an analytical zero-buoyancy plume model to investigate the effects of adjusting entrainment rate and evaporation rate on vertical atmosphere profiles in a simple theoretical framework. Our solutions of the zero-buoyancy plume model suggest that stronger horizontal mixing can lead to larger convective updraft mass flux, consistent with the analysis in numerical simulations. We also observe the likelihood of atmospheric profiles converging at a grid size of approximately 100m, potentially as a result of converging entrainment rate and mixing strength. These insights have implications for global storm-resolving simulations, implying a possible convergence of high cloud and deep convection properties as the horizontal resolution approaches around 100m.

Plain Language Summary

High, anvil-shaped clouds in the tropics significantly impact our climate, but simulating them accurately is challenging. Our study reveals that the area these clouds cover in simplified simulations is largely affected by the level of detail in representing the tropical atmosphere. As we refine the simulation resolution, cloud evaporation and the rate of mixing between cloudy and clear air (entrainment) increase, leading to more vigorous updrafts and higher upward mass transport at the level of these high clouds. Consequently, we observe more coverage of high clouds as the simulation resolution improves. Our research indicates that to achieve more realistic cloud simulations, we need to factor in how these processes change with resolution. We expect that the properties of these clouds will begin to converge in the simulations when the grid size reaches approximately the order of 100m.

1 Introduction

Simulating cloud and convection accurately has long been a major challenge for accurate climate and weather simulations. Uncertainty associated with cloud remains as one of the most significant factors contributing to climate feedback uncertainties in future climate change projections (e.g., Bony et al., 2015; Zelinka et al., 2020). In recent years, the scientific community has made significant strides in developing and examining global storm-resolving models (GSRM) with grid sizes of 1-5km (e.g., Satoh et al., 2019; Stevens et al., 2019). By explicitly resolving deep convection, GSRMs can bypass the uncertainties in convective parameterization. A crucial question for using the GSRMs is whether a resolution at the order of 1km is sufficient to resolve relevant atmospheric physical processes.

Resolution dependence in atmosphere models that explicitly resolve deep convection has been extensively studied in various simulation setup. By changing horizontal grid size from 80km to 2.5km in a GSRM, Hohenegger et al. (2020) showed that many 40-day mean, global mean climate statistics, such as precipitation, sensible heat flux, and outgoing longwave radiation, exhibit weak resolution dependence compared with the uncertainties across different GSRMs. However, Hohenegger et al. (2020) also showed some convection and cloud properties, such as the width of the Intertropical Convergence Zone and the fraction of deep convective clouds, have not converged even at 2.5km resolution. Miyamoto et al. (2013) also examined the sensitivity of deep convection to resolution at

around the order of 1km in global simulations. They showed that deep convective cores start to occupy more than one grid point at around 2km and have stronger upward velocity with finer resolution. In idealized squall line simulations, Bryan et al. (2003) showed decreasing grid size from the order of 1km to the order of 100m tends to give more turbulent flow with resolved entrainment and overturning within clouds. In limited-area 24-hour simulations with tropical maritime large-scale forcing, Khairoutdinov et al. (2009) found low sensitivity of quantities such as cloud fraction, relative humidity, and precipitation rate to grid size ranging from 100m to 1600m, but updraft core statistics are senstive to resolution, with finer resolution showing larger upward velocity and more total water in updraft core. From limited-area radiative-convective equilibrium (RCE) simulation studies, Jeevanjee (2017) showed that the updraft velocity can keep increasing with finer resolution until grid size is at the order of 100m. Jeevanjee and Zhou (2022) found that, in RCE simulation, high cloud fraction exhibits strong resolution dependence, with finer resolution leading to higher anvil cloud fraction.

In the present study, we focus on the resolution dependence of anvil cloud fraction in RCE simulations. Anvil cloud plays a crucial role in regulating the atmospheric radiation flux, but large uncertainties remain in the modeling of anvil clouds. In a study from an intermodel comparison project of RCE simulations (Wing et al., 2020), even under very similar setups, different models produce very different anvil cloud fraction and disagree on the sign of anvil cloud fraction change with warmer sea surface temperature. Sherwood et al. (2020) reported that cloud feedback uncertainty associated with anvil clouds is comparable to other types of clouds such as tropical marine low clouds. Anvil cloud fraction could be thought of as the product of mass detrainment and lifetime of detrained clouds (e.g., Seeley et al., 2019; Beydoun et al., 2021). The mass detrainment describes how fast cloud mass is ejected into the atmosphere from deep convective core. The mass detrainment is closely related to the mass flux of convective updrafts reaching the upper troposphere. The lifetime describes how long the detrained cloud mass can stay in the atmosphere before removed by evaporation/sublimation and sedimentation. The lifetime can be sensitive to microphysics parameterization used in the model (e.g., Hartmann et al., 2018). Different microphysics schemes can lead to very different anvil cloud fraction (e.g., see our results in later sections).

Jeevanjee and Zhou (2022) (hereafter, JZ22) showed a striking dependence of anvil cloud fraction on horizontal resolution. In their simulations, they observed that the peak anvil cloud fraction rises dramatically from approximately 5% at the coarsest 16 km grid size to over 40% at the finest 62.5 m resolution, with no indication of convergence even at this highest resolution. They argued that finer horizontal resolution corresponds to stronger mixing with a shorter mixing timescale, which they defined as the time for a cloudy grid to completely mixed with a neighboring clear grid. The stronger mixing can enhance cloud evaporation and lower precipitation efficiency. A smaller precipitation efficiency would then lead to greater cloud based mass flux, which would lead to more mass flux reaching upper troposphere and producing more anvil clouds.

While the findings in JZ22 offer significant insights, it is intriguing to note the differing results presented by Bogenschutz et al. (2023). Specifically, they observed that during a 20-day simulation with observed large-scale forcing, the anvil cloud fraction is insensitive when the resolution changes from 5km to 500m, whereas in JZ22 the anvil cloud fraction does not converge even at a grid size of 62.5m. The duration of the simulation and the presence or absence of large-scale forcing could be influential factors. Notably, JZ22 ran simulations over a longer period (50 days) to achieve radiative-convective equilibrium, without including any large-scale forcing. Furthermore, differences in microphysics and sub-grid turbulence parameterization used in the two studies might also contribute to the different sensitivity of high clouds.

In this study, we would like to further examine the causality in the argument in JZ22 that enhanced mixing with finer resolution can lead to more convective updraft mass

flux in the upper troposphere through increased precipitation efficiency and increased cloud base mass flux. Jeevanjee (2022) showed that the increase in cloud base mass flux due to higher precipitation efficiency is not entirely robust, given the unconstrained effects of entrainment and detrainment. It is also not clear whether changes in cloud base mass flux can consistently project to the upper troposphere, again considering the unconstrained effects of entrainment and detrainment.

We tested the resolution dependence of anvil cloud fraction in small-domain RCE simulations with grid size ranging from 4km to 125m. The domain size is fixed across different simulations. Since the anvil cloud fraction is sensitive to microphysics parameterization, we examined the mechanism for the resolution dependence in two different microphysics schemes. We found that anvil cloud fraction shows sign of convergence when the grid size is at the order of 100m. Consistent with JZ22, due to enhanced horizontal mixing, finer resolution produces more updraft mass flux in the upper troposphere and leads to increasing anvil cloud fraction. The stronger mixing in finer resolution leads to enhanced cloud evaporation and stronger entrainment rate. By examining the clear-sky energy budgets, we showed that both the enhanced cloud evaporation and the stronger entrainment rate could contribute to a stronger environmental subsidence and updraft mass flux.

We further used an analytical zero-buoyancy plume model to examine the effects of changing evaporation rate and entrainment rate in a simple theoretical framework. We refined the plume model and derived self-consistent solutions of RCE atmosphere profiles. We found that increasing entrainment rate can lead to increase of upper troposphere mass flux through either more cloud evaporation or weaker stability in the upper troposphere. However, increasing evaporation rate alone may not necessarily change the updraft mass flux in the upper troposphere. The insights from the analytical plume model emphasize the role of the horizontal mixing and refine the pathway connecting enhanced mixing to a stronger upper tropospheric mass flux.

The rest of the manuscript is structured as follow: in section 2 we describe the experimental setup. Section 3 shows our results. Section 3.1 shows the contribution of mass detrainment and lifetime to the cloud fraction changes. Section 3.2 shows how the stronger mixing in finer resolution simulations contributes to more updraft mass flux through energy balance. Section 3.3 shows the results and insights from the analytical solution of the zero-buoyancy plume model. Section 4 is the discussion and summary.

2 Experiment setup

We use the System for Atmosphere Modeling (SAM; Khairoutdinov & Randall, 2003), version 6.10.6, configured as a cloud-resolving model. We run three-dimensional RCE simulations using the same domain size of 128km×128km with different horizontal resolution of 4km, 2km, 1km, 500m, 250m, and 125m. All simulations use 60 vertical levels with model top located at 26km and a rigid-lid top boundary condition. The vertical grid spacing increases from 75m near the surface to a constant of 500m throught the whole free troposphere and above. A sponge layer is located in the upper 30% of the model domain (i.e., above 18km). The radiation scheme is Rapid and Accurate Radiative Transfer Model for General Circulation Models (RRTMG) (Iacono et al., 2008). A simple Smagorinsky-type scheme (Khairoutdinov & Randall, 2003) is used for the effect of subgrid-scale motion. We use a constant solar insolation (no diurnal cycle) with fixed solar constant of 683.5 $W\,m^{-2}$ and zenith angle of 50.5°. Domain-averaged horizontal wind is nudged to zero at each vertical level with a nudging time scale of 1hour. Sea surface temperature is fixed uniformly at 303K.

We use two different microphysics schemes: SAM single-moment scheme (SAM1MOM, Khairoutdinov & Randall, 2003) and a double-moment Morrison scheme (Morrison et

al., 2005). The SAM one-moment scheme uses an instantaneous saturation adjustment to generate and remove cloud condensate. Between 0° and -20°C, partitioning of cloud condensate into cloud ice and liquid water depends linearly on temperature (at -20°C, all condensate is ice; at 0°C, all condensate is liquid water). More pathways for conversion between different hydrometeors are included in the Morrison double-moment scheme. The Morrison scheme tends to produce more ice cloud in the upper troposphere (e.g., Powell et al., 2012; Hu et al., 2021) and consequently strong atmospheric cloud radiative heating in the middle and upper troposphere. This stronger atmospheric cloud radiative heating can stabilize the upper troposphere and weaken the convective updraft reaching the upper troposphere (Hu et al., 2021). As we will show later, the weaker upper troposphere mass flux will lead to less cloud evaporation in the environment in the Morrison scheme than in the SAM1MOM scheme.

For the simulations with horizontal resolution from 4km to 250m, the first 50 days are taken as the model spinup and considered long enough for the model to reach equilibrium. After the 50-day spinup, a 20-day post-equilibrium period is used for analysis. The 30 samples-per-hour data are then averaged to get an hourly output of domain-mean statistics. For the 125m-resolution simulation, we initialize the simulation with the equibirium temperature and moisture profile from the 500m-resolution simulation. Then we run only 30 days for spinup and another 20 days for analysis.

3 Results

3.1 Cloud fraction change due to mass detrainment

Fig. 1 illustrates the resolution-dependent behavior of cloud fraction, atmospheric cloud radiative effects, and relative humidity. A grid is classified as cloudy if the cloud mass (the sum of ice and liquid water) mixing ratio exceeds 10^{-5} kg kg^{-1}. As the grid spacing decreases from 4km to 125m, the peak anvil cloud fraction increases from 7.5% to 13% in the SAM1MOM simulations (Fig. 1a) and from 17% to 27% in the Morrison simulations (Fig. 1d). This amplified cloud fraction subsequently leads to increased cloud radiative heating throughout the majority of the free troposphere (Fig. 1b and 1e). The cloud fraction profiles appear to converge when the grid spacing falls below 250m in the SAM1MOM simulations. Along with the increase of the cloud fraction, both the SAM1MOM and Morrison simulations exhibit a rise in relative humidity throughout the entire free troposphere with finer resolution (Fig. 1c and 1f).

Anvil cloud fraction can be diagnosed as the product of mass detrainment and cloud lifetime (e.g., Seeley et al. 2019, Beydoun et al. 2022). In Fig. 2, we present profiles of convective updraft mass flux and in-cloud sedimentation rate to look at the change of mass detrainment and lifetime change. The convective updraft is characterized by grids with a vertical velocity greater than 1 m s^{-1} and a cloud mixing ratio exceeding 10^{-5} kg kg^{-1}. The in-cloud sedimentation rate is defined as $qcsed/qc$ averaged over cloudy grids, where qc is the cloud mass (ice plus liquid water) mixing ratio and $qcsed$ is the tendency of qc due to sedimentation of cloud ice. This sedimentation rate is the major term of the net removal rate in Beydoun et al. 2022 and could be interpreted as one over lifetime. Sedimentation rate is positive above around 10 km and negative below, representing cloud ice falling from detraining level downwards. In both the SAM1MOM and Morrison simulations, the convective updraft mass flux at above 11km increases with higher resolution, signifying an increased vertical mass convergence above this altitude. By mass continuity, the increase of vertical convective mass flux convergence corresponds to an increase of mass detrainment and an increase of horizontal mass convergence in clear-sky region. The convective updraft mass flux at middle and lower troposphere shows non-monotonic change. This is partly due to increased cloud radiative effects with finer resolution, which may stablize the middle troposphere. The sedimentation rate is weaker for finer resolutions in the SAM1MOM scheme but is slightly stronger in the Morrison

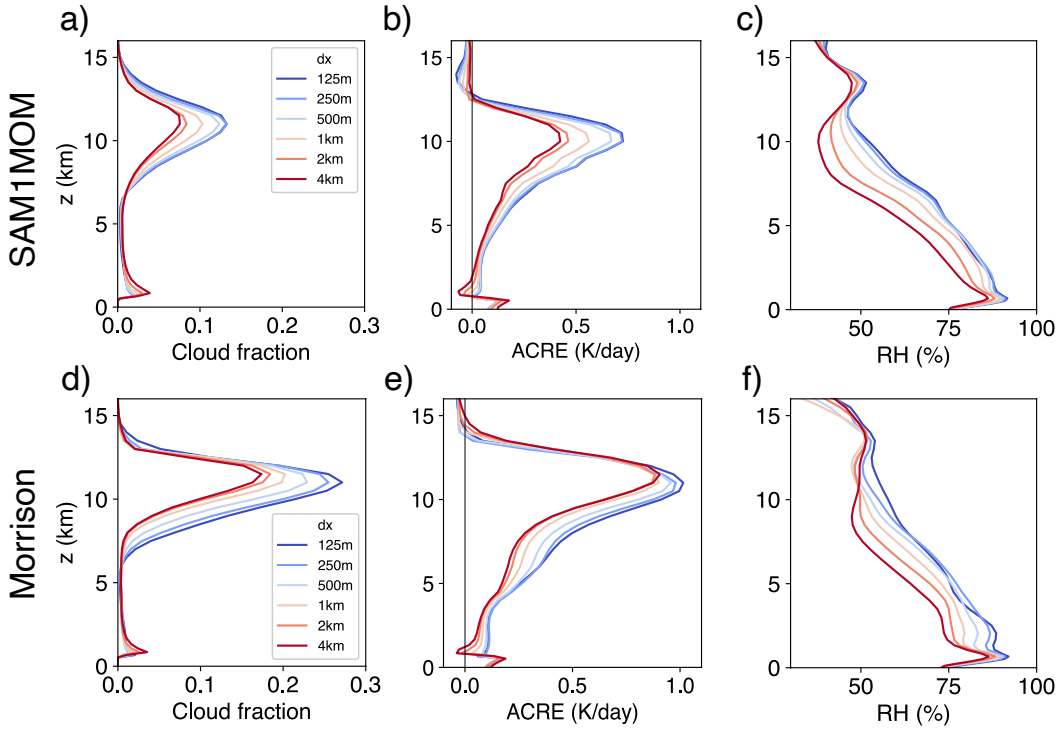

Figure 1. Domain-mean steady-state profiles of cloud fraction (left column), atmosphere cloud radiative effects (middle column) and relative humidity (right column). The upper row corresponds to the SAM1MOM simulations, while the lower row represents the Morrison simulations. Different colors indicate varying grid sizes, with warmer colors denoting coarser resolutions.

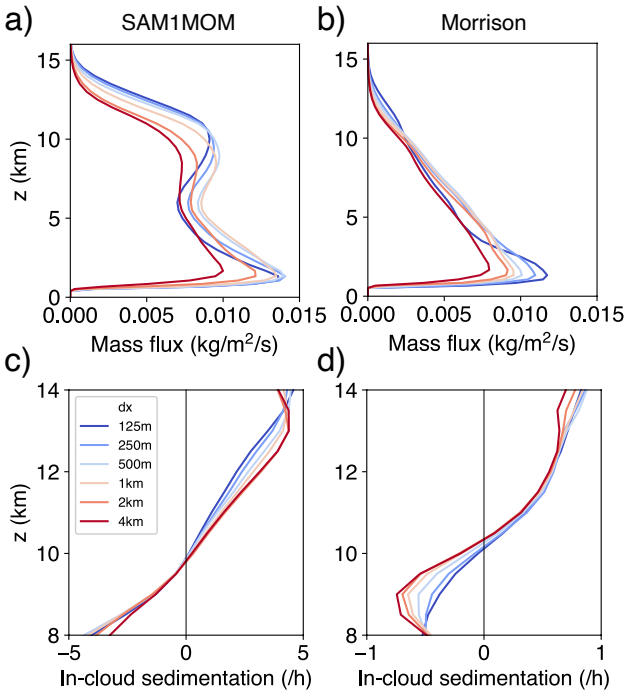

Figure 2. Domain-mean steady-state profiles of convective updraft mass flux (upper row) and cloud ice sedimentation rate (lower row). The left column corresponds to the SAM1MOM simulations, while the right column represents the Morrison simulations. Different colors indicate varying grid sizes, with warmer colors denoting coarser resolutions.

scheme. Hence, the observed increase in cloud fraction with finer resolution in both SAM1MOM and Morrison simulations is predominantly driven by the amplification of mass detrainment. The contribution from lifetime changes is less certain and could be contingent on the microphysics schemes employed.

3.2 Budgets for environmental subsidence

In this section, we investigate the mechanisms responsible for the increase in convective updraft mass flux associated with finer resolutions. According to the principle of mass continuity, the mass flux in convective updrafts must be balanced by subsidence in the surrounding environment, which we define as grids possessing a cloud mixing ratio less than 10^{-5} kg kg^{-1}. Consequently, elucidating changes in convective updrafts necessitates a corresponding understanding of changes to environmental subsidence. By employing the dry static energy budget of the environment, we decompose the subsidence and will demonstrate that modifications to mass flux profiles could be attributed to changes in both cloud evaporation rate and entrainment rate. The changes in cloud evaporation and in entrainment rate are not purely independent as the change of horizontal mixing can influence both of them. The relative contribution of these two factors will be elaborated upon in the subsequent section.

The dry static energy is defined as $s = c_p T + gz$. The conservation of dry static energy requires

$$\frac{\partial s}{\partial t} + \vec{u} \cdot \nabla_h s + w \frac{\partial s}{\partial z} = Q_{rad} + Q_{lat} \tag{1}$$

where Q_{rad} is radiative heating, and Q_{lat} is latent heating in the environment. By averaging over all environmental grids and time, and ignoring the time tendency, we obtain:

$$\langle \vec{u} \cdot \nabla_h s \rangle + \langle w \frac{\partial s}{\partial z} \rangle = \langle Q_{rad} \rangle + \langle Q_{lat} \rangle \tag{2}$$

After further decomposition of $\langle w \frac{\partial s}{\partial z} \rangle = \langle w \rangle \langle \frac{\partial s}{\partial z} \rangle + \langle w' \frac{\partial s'}{\partial z} \rangle$, the averaged environmental subsidence can be expressed as:

$$\langle w \rangle = \frac{\langle Q_{rad} \rangle}{\langle \frac{\partial s}{\partial z} \rangle} + \frac{\langle Q_{lat} \rangle}{\langle \frac{\partial s}{\partial z} \rangle} - \frac{\langle \vec{u} \cdot \nabla_h s \rangle}{\langle \frac{\partial s}{\partial z} \rangle} - \frac{\langle w' \frac{\partial s'}{\partial z} \rangle}{\langle \frac{\partial s}{\partial z} \rangle} \tag{3}$$

This equation essentially encapsulates the energy balance within the environment, implying that the subsidence heating is counterbalanced by the cooling induced by radiation and phase changes in water. In Fig. 3, we show the profiles of latent-driven and radiation-driven subsidence for the SAM1MOM simulations. The combined effect of latent- and radiation-driven subsidence closely mirrors the subsidence deduced from model output, and the contribution of advection terms appears minor in comparison to the contribution of radiation and latent heating (not shown).

The subsidence near anvil level increases with finer resolution (Fig. 3a), which is consistent with the change of convective updraft mass flux. In the SAM1MOM simulations, a large portion of the increasing subsidence is counteracted by the negative latent heating in the environment due to evaporation and sublimation of clouds (Fig. 3b). Conversely, negative radiative heating accounts for a relatively smaller portion of this balance (Fig. 3c). The relative contribution of latent and radiative heating in the Morrison scheme is somewhat different. We will probe into the nuances of the Morrison simulations later in this section. It is important to underscore that the role of latent heating can be influenced by the specific definition of "environment". In our study, the environment, defined as grids with a cloud mixing ratio less than 10^{-5} $\mathrm{kg\,kg^{-1}}$, incorporates grids distanced from clouds as well as those in close proximity to clouds, which experience evaporation and sublimation from cloud. Results in the following paragraphs are not sensitive to the choice of cloud threshold. Changing the threshold from 10^{-5} $\mathrm{kg\,kg^{-1}}$ to 10^{-7} $\mathrm{kg\,kg^{-1}}$ results in little change. Such insensitivity might be attributed to the model's procedural steps, wherein evaporation is calculated prior to the output of the cloud mixing ratio. Consequently, grid cells can reflect marginal cloud mixing ratios while still indicating evaporation in the resultant data.

The change of latent-driven subsidence is consistent with the change of latent heating in the environment (Fig. 3d). In the upper troposphere the cooling from phase change is primarily associated with cloud evaporation/sublimation (Fig. 3e). For simplicity, we will henceforth use the term "evaporation" to refer to both the evaporation of cloud water and sublimation of cloud ice. The cooling due to re-evaporation of precipitation, which is not displayed here, is less significant than that of clouds in the upper troposphere, although it presents a similar strength in the lower troposphere. We have shown that a finer resolution model tends to generate more clouds and updraft mass flux. Therefore, the observed increase in latent cooling might be simply a consequence of the larger amount of clouds available for evaporation. However, an interesting observation arises when we normalize the cooling due to cloud evaporation by the domain mean cloud mass mixing ratio (Fig. 3f). Domain mean cloud mixing ratio is proportional to the total cloud mass in each layer. It becomes evident that, per unit mass, clouds tend to induce a greater amount of cooling in the environment in the upper troposphere (and also in lower altitudes) when modeled at finer resolution.

The observed enhancement in evaporation could be associated with the model resolution through the geometric representation of cloud boundaries. We will use clouds at anvil level as an example, but we assume the intuition behind should apply to clouds at

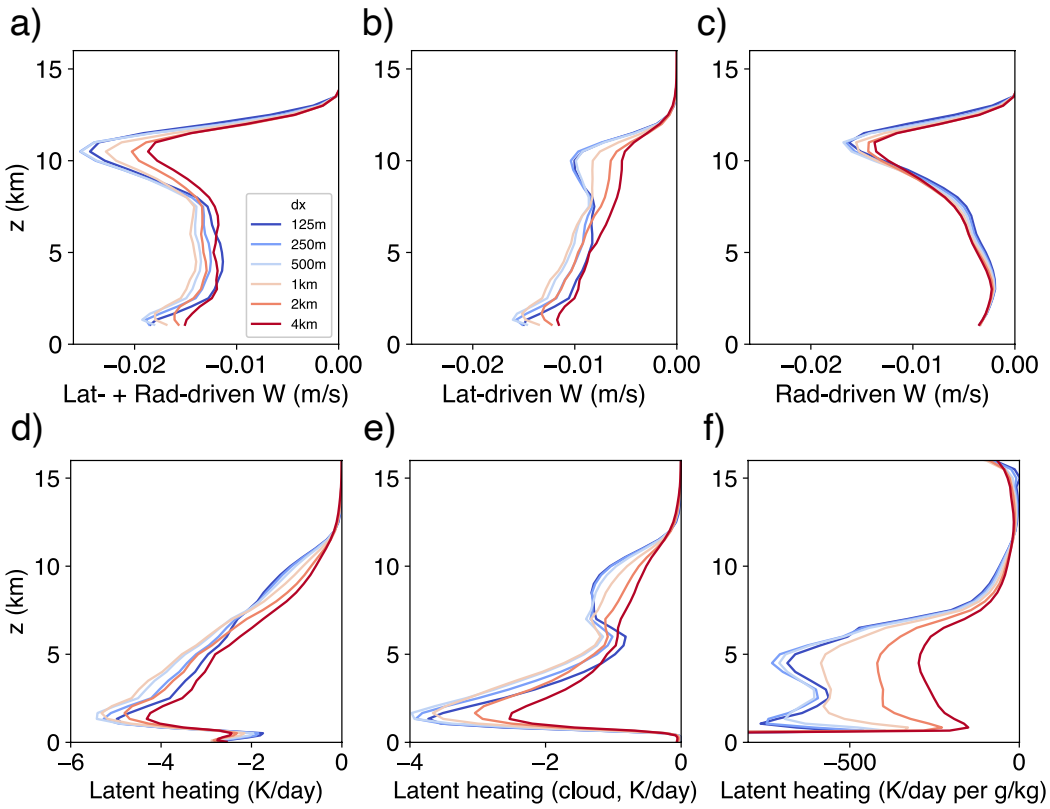

Figure 3. Energy budget for environmental subsidence for the SAM1MOM simulations. The first row shows the subsidence contributed by latent heat (panel b), by radiative cooling (panel c), and by both (a). Panel d shows the latent heating rate averaged in environments. Panel e shows the latent heating rate associated with the phase change between clouds and vapor averaged in environments. Panel f normalizes the cloud-related latent heating rate in panel e by the domain-mean cloud mixing ratio.

all the levels. Horizontal snapshots of the cloud mixing ratio at an altitude of z=10km are depicted in Fig. 4a and 4b. These images represent two 32km×32km subdomains in the 4km-resolution and 125m-resolution simulations respectively. When compared to the clouds in the coarser 4km-resolution simulation, the clouds in the 125m-resolution simulation exhibit more complex boundary structures and tend to be more dispersed. As a result, clouds modeled at finer resolutions exhibit a higher perimeter area ratio (Fig. 4c). In other words, for a cloud patch of the same area, the total perimeter will be longer in the simulation with finer resolution. This effect is somewhat analogous to the coastline paradox in fractal geometry, where the measured length of a coastline varies depending on the scale of measurement. The increased perimeter to area ratio exposes a larger mass of the cloud to the environment, potentially leading to greater evaporation near the cloud edges.

The study by Siebesma and Jonker (2000) explored the fractal nature of cumulus clouds in Large-Eddy Simulations. They argued that while a coarse grid will underestimate cloud surface area, the total sub-grid turbulent transport could become resolution independent if the grid size is within the inertia subrange. However, in our simulations with a grid size on the order of 1km, sub-grid diffusion in the free troposphere is minimal. We observed that turning off horizontal sub-grid diffusion of scalars (such as energy and water) resulted in only minor changes to the profiles of cloud fraction and environmental evaporation (not shown). The cloud evaporation of deep convection is substantially influenced by numerical diffusion and can be enhanced by a larger perimeter-to-area ratio. To illustrate this point, we derived an equation (see Appendix A for complete derivation) that describes the relationship between cloud evaporation in relation to resolved advection and the perimeter-to-area ratio:

$$\frac{Q_{lat,env}}{q_m} = \frac{L}{A} U_{adv} \frac{q_{c,edge} + q^*_{v,env}(1 - RH)}{q_{cld}} \frac{L_v}{2c_p f_{env}} \tag{4}$$

The Equation 4 indicates that the evaporation due to horizontal mixing at cloud edges is dependent on several factors. These include the perimeter-to-area ratio (L/A), the resolved horizontal velocity near the cloud edge (U_{adv}), the cloud mixing ratio near the cloud edge ($q_{c,edge}$), the saturation deficit in the environment ($q^*_{v,env}(1-RH)$), and the average cloud mixing ratio within cloudy grids (q_{cld}). We verify this equation at the anvil level, characterized by relatively weak vertical motion near the cloud edge, hence, making cloud evaporation predominantly attributable to horizontal mixing. Fig. 4d demonstrates that the diagnosed evaporation using Equation 4 qualitatively aligns with the direct model output. From this equation, it is evident that an increased perimeter to area ratio can positively contribute to enhanced cloud evaporation. In Appendix A, we delve into how other terms in Equation 4 vary with model resolution. It is more difficult to validate Equation 4 at lower levels. In the middle troposphere, clouds are typically very close to the convective core, and evaporation/condensation associated with vertical motion may not be neglected. However, we assume the enhanced horizontal mixing and larger perimeter area ratio should still positively contribute to the enhanced evaporation we show in Fig. 3f. It is important to note the importance of enhanced horizontal mixing occurring at all levels, not solely at the anvil level. More efficient evaporation at lower levels could contribute to mass flux increase at those levels and, by mass continuity, should have a continuing influence on mass flux at higher levels.

In the Morrison simulations, we also observe an enhancement in subsidence near the anvil level, as shown in Fig. 5a. However, the contribution from latent-driven subsidence (Fig. 5b) is weaker in the Morrison scheme compared to the SAM1MOM scheme. Primarily, the subsidence change near anvil level is dominated by radiation-driven subsidence (see Fig. 5c). We will discuss more on the reasons for the diminished latent-driven subsidence near anvil level in the Morrison simulations at the end of this section.

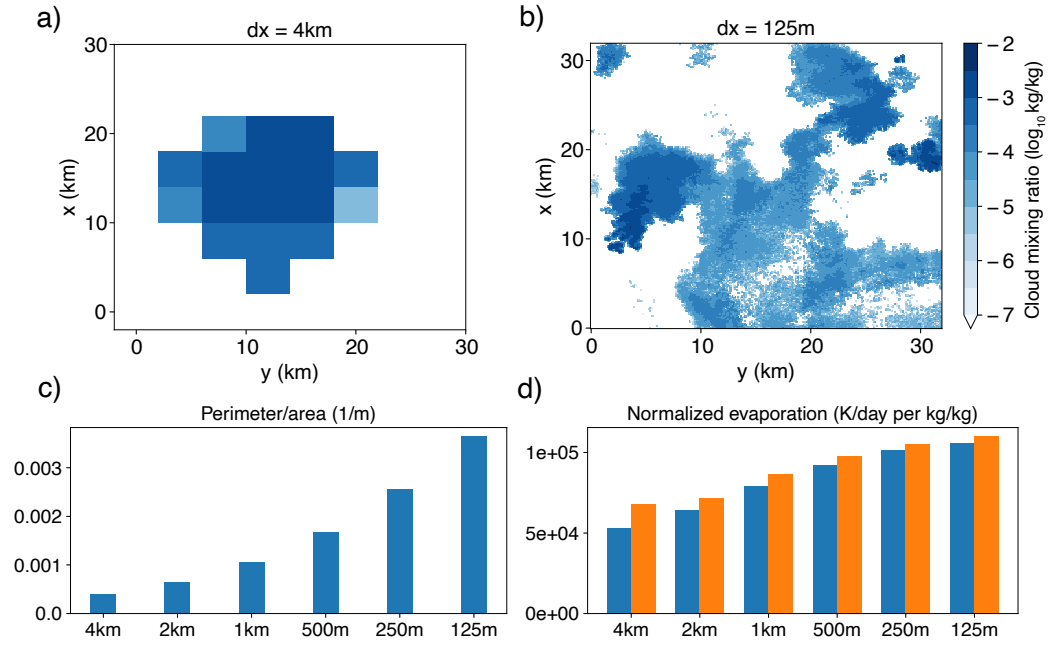

Figure 4. The upper row shows the cloud mixing ratio snapshots at z=10km in a 32km×32km subdomain in the SAM1MOM simulations with grid size of 4km (a) and 125m (b). Panel c shows the perimeter area ratio in the SAM1MOM simulations with different grid size. Panel d shows the normalized evaporation in Fig. 3f at z=10km. Blue bars are direct model diagnostic values, and orange bars are estimated by Equation 4.

We further dissect the radiation-driven subsidence into radiation and stability components. The radiative cooling shows slight non-monotonic changes (Fig. 5d), while the upper troposphere is less stable with finer resolution (Fig. 5e and 5f). The change in stability can be associated with the shift in the entrainment rate (Fig. 6), which tends to increase with finer resolution. We illustrate this entrainment change with a model of a spectrum of entraining plumes, following the approach of Kuang and Bretherton (2006). In this spectrum plume calculations, we use environmental profiles from each simulation to infer the entrainment rate for updrafts. In Fig. 6a and 6c, we show the convective updraft mass flux distribution in the space of frozen moist static energy (FMSE) and height. FMSE is defined as $c_pT + gz + L_vq - L_fq_i$. The individual lines represent the FMSE profiles of entraining plumes rising from the cloud base with different entrainment rates. The convective updrafts in the 125m-resolution simulation (Fig. 6c) shift towards FMSE profiles with higher entrainment rate compared to the updrafts in the 4km-resolution simulation (Fig. 6a). Once we have computed the FMSE profiles with varying entrainment rates, we can measure the amount of mass flux allocated to each entrainment rate bin. Subsequently, we can represent the updraft mass flux in the space of height and entrainment rate. As shown in Fig. 6b and 6d, it is apparent that the mass flux distribution shifts towards higher entrainment rates with finer resolution. We have done similar analysis for the SAM1MOM simulations (not shown) and found consistent results that finer resolution tends to have higher entrainment rates. However, it is important to note that the sensitivity of entrainment rate on grid size could be model dependent. In the SAM model we use, the entrainment mixing seems to be contributed mainly by numerical diffusion, while sub-grid diffusion is very weak in free troposphere. Whether the resolution dependence of the entrainment rate would hold with other models using different advection scheme and sub-grid diffusion scheme needs to be further tested.

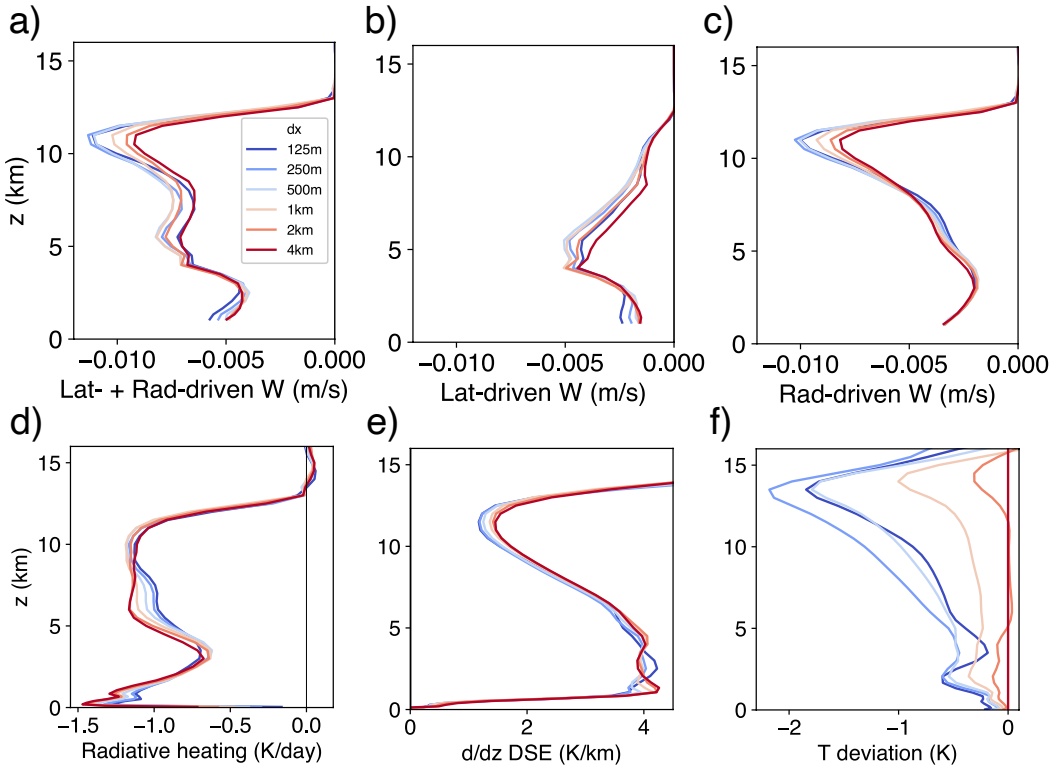

Figure 5. Energy budget for environmental subsidence for the Morrison simulations. The first row shows the subsidence contributed by latent heat (panel b), by radiative cooling (panel c), and by both (a). Panel d shows the radiative heating rate averaged in environments. Panel e shows the vertical gradient of dry static energy averaged in environments. Panel f shows the absolution temperature profiles as deviation to the 4km Morrison simulation.

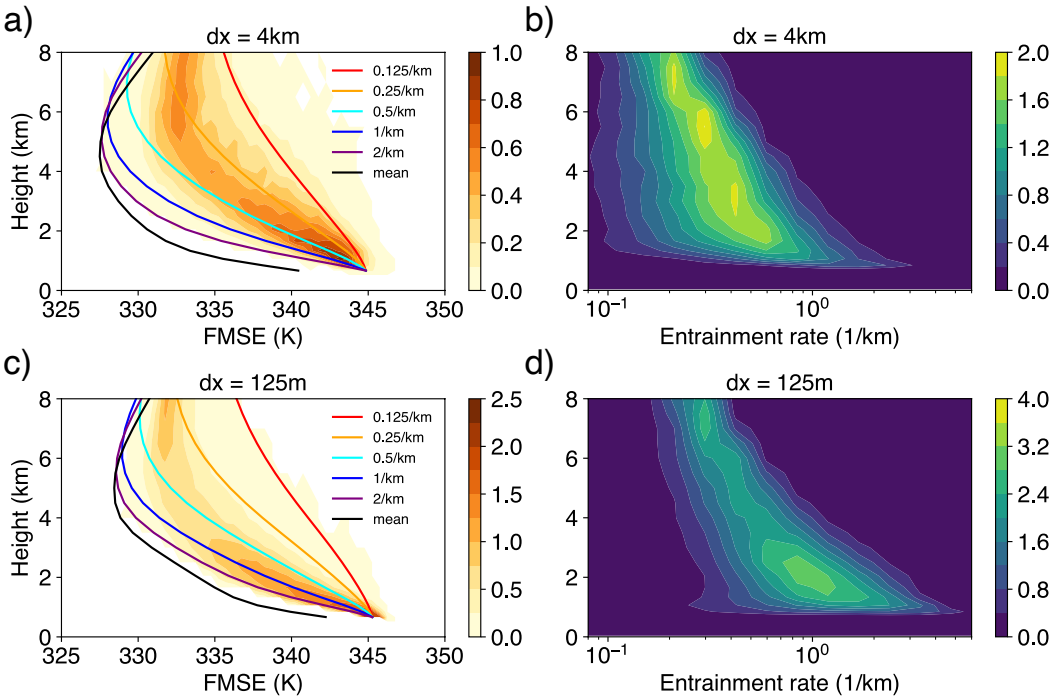

Figure 6. The distribution of convective updraft mass flux in FMSE-height space (left column) and in entrainment-height space (right column) for grid size of 4km (upper row) and of 125m (lower row). In the left column, we show the mass flux distribution (with a unit of a unit of $kg\,m^{-2}s^{-1}bin^{-1}$) binned by their FMSE (in unit of K). There are 50 bins with 0.5K interval between 325K to 350K. The individual lines represent the FMSE profiles of entraining plumes rising from cloud base with different entrainment rates, except the black line which represents domain-mean FMSE profiles. In the right column, we show the mass flux distribution (with a unit of a unit of $kg\,m^{-2}s^{-1}bin^{-1}$) binned by their effective entrainment rate. The bin boundaries have entrainment rates of $2^{(i/2)-4}$, for $i = 0, 1, 2, ..., 16$, with a unit of km^{-1}. We calculated the instantaneous FMSE profiles with these different entrainment rates and sorted the convective updraft mass flux by these different entraining moist-adiabat FMSE values.

Fig. 7 explores the reasons behind the distinctive environmental energy balance regime observed in the Morrison simulations compared to the SAM1MOM simulations. In the Morrison simulations, the cooling effect from evaporation in the upper troposphere is notably weaker than that from radiation. Two factors could account for this subdued evaporation: diminished updrafts and a slower evaporation rate. As previously noted, the Morrison scheme tends to generate more anvil clouds, probably due to the significantly slower ice sedimentation removal rate and prolonged lifetime (refer to Fig. 2). The enhanced cloud radiative heating in the Morrison simulations could stabilize the upper troposphere, thereby reducing the intensity of updrafts. When we disable cloud radiative effects in the Morrison simulations (represented by solid lines in Fig. 7), we observe an increase in upper troposphere convective updrafts and stronger latent-driven subsidence, compared to the default Morrison simulations (dotted lines in Fig. 7). Additionally, the Morrison scheme does not employ saturation adjustment for cloud ice, potentially slowing evaporation compared to the SAM1MOM scheme. When we deactivate the cloud radiative effect and accelerate the cloud ice sublimation rate 100 times to mimic the saturation adjustment (dashed lines in Fig. 7), the result is faster evaporation and intensified updrafts. Consequently, latent-driven subsidence now contributes comparably to radiation-driven subsidence in modifying total subsidence near anvil level as resolution becomes finer (see Fig. 7b to d).

3.3 Insights from an analytical plume model

In the previous section, we presented that stronger horizontal mixing in finer-resolution simulations can enhance cloud evaporation and weaken the stability through a stronger entrainment rate. Both factors could potentially contribute to an enhanced convective updraft mass flux through the energy balance of environmental subsidence. However, a budget analysis does not necessarily reveal causality. Thus, in this section, we employ an analytical plume model to qualitatively explore the separate causal effects of changes in cloud evaporation and entrainment. This dissection of entrainment and evaporation effects offers us the opportunity to refine our understanding of the mechanism that bridges horizontal mixing with convective updraft mass flux.

The analytical plume model we use here is adapted from the zero-buoyancy plume model in Singh and Neogi (2022), with further references to Romps (2014), Singh et al. (2019), and Romps (2021). Here we provide a brief description of the model setup with the full description in Appendix B. The model presented in Singh and Neogi (2022) includes a thermodynamic component and a dynamic component. The thermodynamic component solves the equilibrium state of a moist atmosphere, and the dynamic component couples the thermodynamic component to large-scale circulation. In this study, we utilize only the thermodynamic model to examine radiative-convective equilibrium with no large-scale vertical velocity. It's crucial to distinguish between the analytical plume model used in this section and the spectrum plume model used for calculating the entrainment rate in the previous section. The latter utilizes the environmental profile from each simulation to determine a spectrum of entrainment rates for updrafts. Conversely, the analytical plume model in this section solves for the environmental profiles based on given surface boundary conditions and specified mixing strength and evaporation rate.

The thermodynamic model assumes that the steady state of the atmosphere can be represented by updrafts in a single updraft plume and downdrafts in environment. The updraft and environment can exchange mass, water, and heat via entrainment and detrainment. The model assumes that the steady state of the atmosphere is neutrally buoyant with respect to the entraining plume (Singh & O'Gorman, 2013). The model further presumes that the radiative cooling rate is a function of temperature, i.e., $-1K\,day^{-1}$ when the temperature is above 250K, and gradually decays to 0 at 200K. By solving conservation equations of mass, water vapor, and moist static energy, this model can solve the vertical atmosphere profiles given surface boundary conditions.

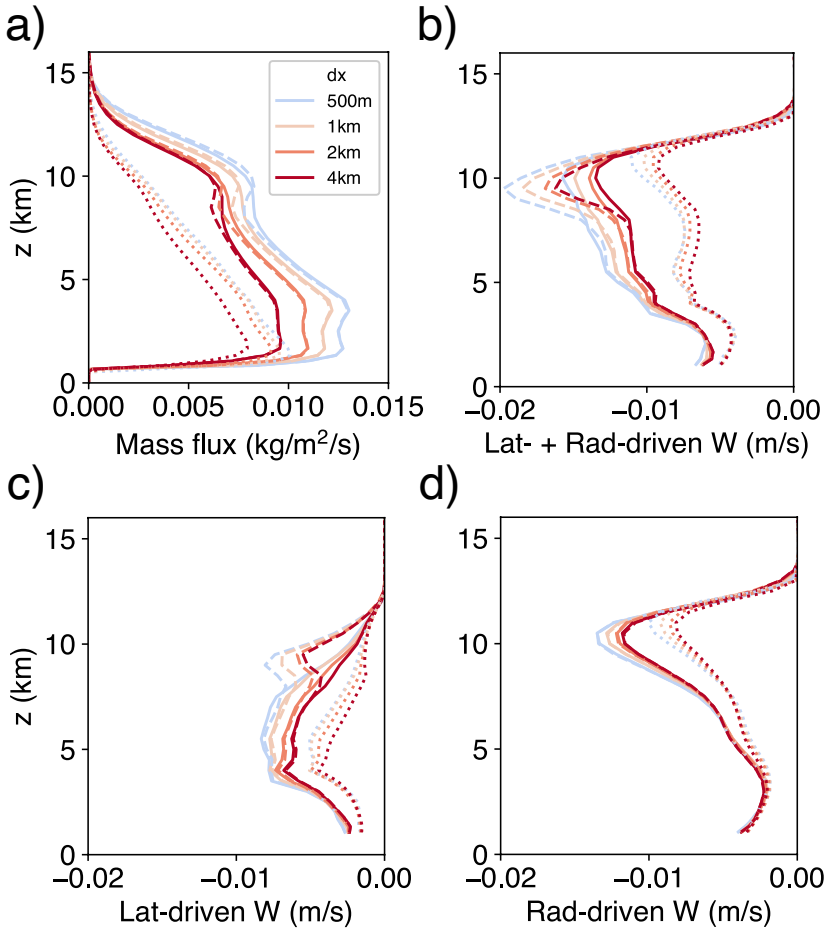

Figure 7. Convective updraft mass flux and energy budget for environmental subsidence in modified Morrison simulations. Solid lines represent simulations where cloud radiative effects are deactivated. Dashed lines indicate simulations with both cloud radiative effects deactivated and expedited cloud ice sublimation. Dotted lines represent default Morrison simulations. Panel a displays the convective updraft mass flux. Panels b to d present the subsidence contributions from latent heat (panel c), radiative cooling (panel d), and a combination of both (panel b).

One caveat of the solutions provided in Singh and Neogi (2022) and Romps (2021) is the assumption of equal fractional entrainment rate and detrainment rate, which in principle should suggest no vertical change in the convective updraft mass flux through the mass conservation equation:

$$\frac{\partial M_c}{\partial z} = M_c(\epsilon - \delta) \tag{5}$$

where M_c is updraft mass flux, ϵ is fractional entrainment rate, and δ is fractional detrainment rate. However, their solution of mass flux profile, e.g., Fig. 7 in Singh and Neogi (2022), does not follow this assumption, especially in the upper troposphere where mass flux rapidly decreases. In this study, we developed a self-consistent method of solving the equations by allowing the difference between fractional detrainment rate and fractional entrainment rate to vary vertically and not imposing any vertically structure on mass flux profile. The shape of the mass flux profile is partially constrained by energetics, as the mass flux needs to diminish where radiative cooling starts to rapidly decrease in the upper troposphere. Therefore, the entrainment rate and detrainment rate cannot be completely independent. Yet, one must still specify the strength of turbulent mixing in the model. This could be represented by either the entrainment rate, detrainment rate, or some other variable, such as the mixing rate in Bretherton et al. (2004). Here we choose to specify the entrainment rate to impose the strength of turbulent mixing. Once we specify the fractional entrainment rate profile (ϵ) and an evaporation parameter (μ), we can determine the vertical atmosphere profiles given boundary conditions (temperature, pressure, and relative humidity at cloud base).

In this model, cloud evaporation is parameterized as:

$$s_{evap} = \mu d(q^* - q) \tag{6}$$

where d is mass detraiment, q^* and q is the specific humidity in saturated updraft and in environment. A larger evaporation parameter μ tends to produce more cloud evaporation in the environment. This equation has two underlying assumptions. First, this equation assumes that the detrained flux of condensate is proportional to detrained flux of water vapor, represented by dq^*. A component of μ quantifies this relationship, representing the amount of condensate present in the detrained air. Second, it assumes that the fraction of detrained condensate that evaporates - as opposed to precipitating to the ground - is proportional to $1-q/q^*$, which equates to $1-RH$. A component of μ quantifies this relationship, reflecting the relative rates of evaporation versus conversion to rain. It is likely that the ratio of condensate evaporation versus conversion to rain is less sensitive to RH when RH is far less than 1. We also explored a different parameterization defined by $s_{evap} = \mu dq^*(1 - RH)^{0.5}$, which yielded results that are qualitatively similar (not shown). The full details of the model equations, derivation of the solution, and some sensitivity tests are documented in Appendix B.

With this model, we now test the sensitivity of the steady-state atmosphere profiles to entrainment rate and evaporation rate. First, we test the sensitivity to the fractional entrainment rate ϵ for two different values of the evaporation parameter μ (Fig. 8, upper row for $\mu = 1$ and lower row for $\mu = 0.1$). In both cases, with an increase in entrainment rate, we observe an increase in detrainment rate, mass flux, relative humidity, and the amount of latent cooling in the environment. The temperature in the upper troposphere is colder with a higher entrainment rate, and the stability (ds/dz) is lower. Fig. 8 suggests that increasing entrainment rate can lead to a relatively uniform increase of mass flux from cloud base to anvil level, although the budget for environmental subsidence can look like different regimes.

Considering the dry static energy budget $M_c = (Q_{rad} + Q_{lat})/(\frac{\partial s}{\partial z})$, increasing entrainment rate leads to both increasing cloud evaporation and more unstable upper troposphere. Both these two factors can contribute to an increasing mass flux. When cloud evaporation is efficient (Fig. 8 with $\mu = 1$), the change of latent cooling can dominate the change of mass flux. However, when cloud evaporation is weak (Fig. 8 with $\mu =$

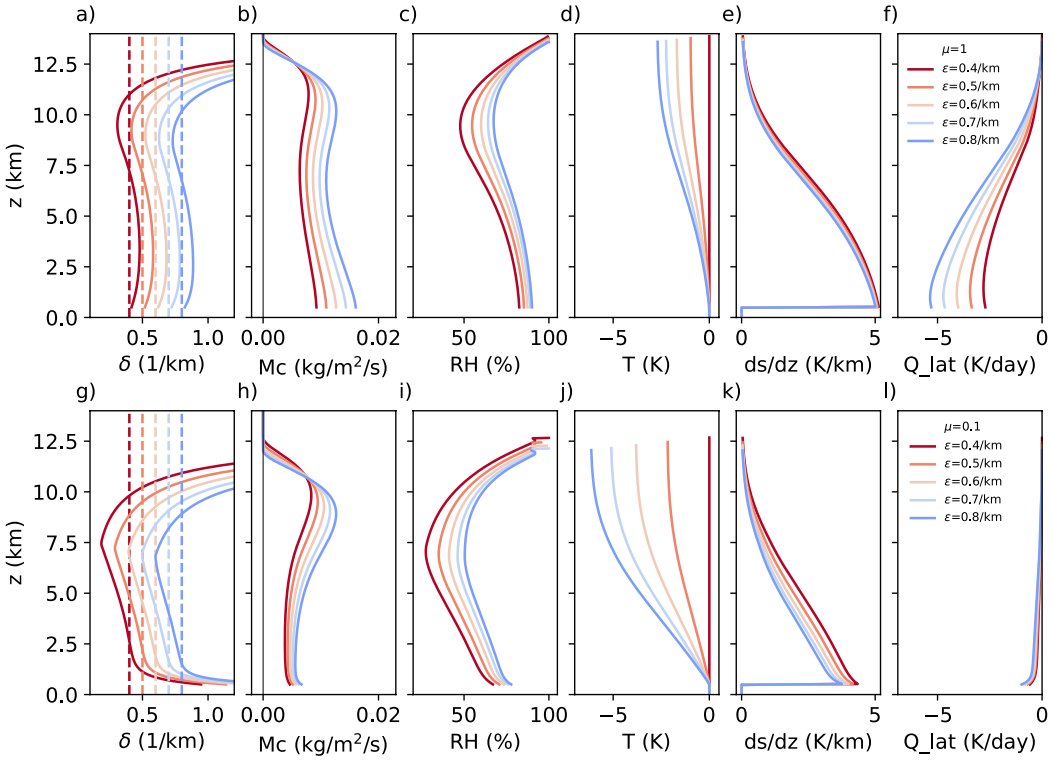

Figure 8. Atmosphere profiles in the zero-buoyancy plume model with varying entrainment rates (warmer color represents lower entrainment rate). The upper row has a cloud evaporation parameter μ=1. The variables shown are detrainment rate (a), updraft mass flux (b), relative humidity (c), temperature (d), vertical gradient of dry static energy (e), and latent heating rate due to cloud evaporation in the environment (f). Dashed lines in panel a are the profiles of prescribed entrainment rate. The temperature in panel d is shown as deviation to one of the simulations, which is denoted by the red line with zero deviation. The lower row is similar to the upper row but with cloud evaporation parameter μ=0.1.

0.1), the absolute latent cooling and the change of latent cooling is small compared to the prescribed radiative cooling. The change of stability to increasing entrainment rate is larger with small μ and can dominate the change of mass flux. Environmental relative humidity is important in determining the sensitivity of stability to changing entrainment rate. The relative humidity is smaller with μ=0.1 than μ=1 (Fig. 8c and i). Since entrainment affects stability through the environmental saturation deficit, a small μ tends to make stability more sensitive to the change of entrainment (Fig. 8e and k).

The energy balance regime with small evaporation parameter resembles that in the Morrison simulations in the previous section. The Morrison scheme likely has a smaller evaporation parameter for cloud ice evaporation than the SAM1MOM scheme, due to the avoidance of saturation adjustment in Morrison scheme, potentially contributing to the weak absolute latent cooling rate. However, the stability change is not that large between Morrison and SAM1MOM scheme, comparing to the difference between the analytical plume results with μ=0.1 and μ=1. The Morrison simulations also have slightly higher relative humidity in the upper troposphere compared to the SAM1MOM simulations. The main difference between the Morrison and the SAM1MOM simulations is the diminished environmental latent cooling instead of the stability change.

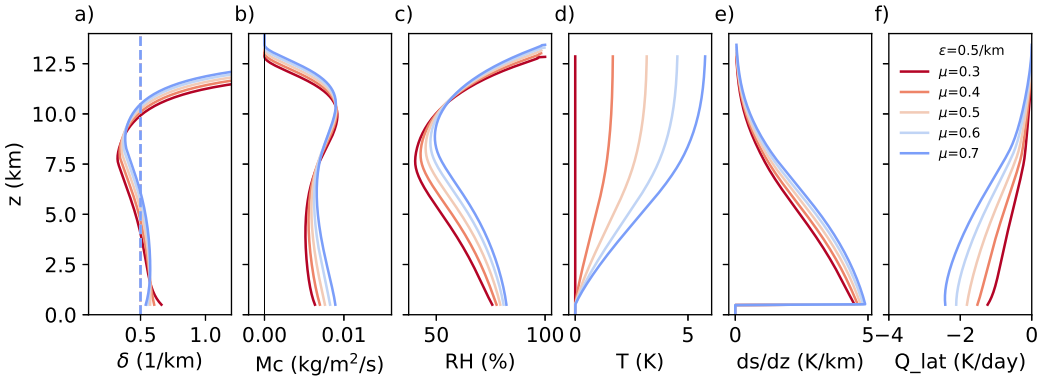

Figure 9. Similar to Fig. 8 but with fixed entrainment rate of 0.5 km^{-1} and varying cloud evaporation parameter (warmer color represents less efficient cloud evaporation).

In Fig. 9, we maintain a constant fractional entrainment rate as 0.5 km^{-1} and test the senvitivity of atmosphere profiles to the evaporation parameter μ. As the evaporation strength increases, we can see that the free troposphere is warmer, deeper, and more moist (Fig. 9b,9c,9d). The increased relative humidity is a direct result of the enhanced efficiency of cloud evaporation. This is consistent with JZ22 which shows that the evaporation efficiency plays an important role for the relative humidity, especially in the upper troposphere. Consequently, with a more moist atmosphere, the dilution of the updraft plume due to entrainment is mitigated, resulting in a warmer and elevated troposphere. In lower troposphere, we see a clear increase of mass flux with increasing cloud evaporation. However, in the upper troposphere, the mass flux adjustment is more akin to a upward shift with weak change in magnitude. The peak mass flux near the anvil level remains largely unchanged, suggesting a minor change in the convergence of mass flux at higher altitudes. From the perspective of the energy budget, an increase in the evaporation rate could induce greater latent cooling. However, this is offset by an increase in stability in the upper troposphere, effectively suppressing the change in mass flux (Fig. 9e and 9f).

From Fig. 8 and Fig. 9, we can see that the resolution dependence of updraft mass flux may not necessarily be driven by evaporation efficiency alone. However, updraft mass flux can simply be interpreted as a response to the change of entrainment rate or the strength of horizontal mixing. In addition to the energy budget, a different way to understand the mass flux response to entrainment rate change in this analytical model is through the Betts's rule described in Jeevanjee (2022). Considering the water vapor budget for the atmosphere above a certain level z. The mass flux at z satisfies:

$$M_c q^*(1 - RH) = \int_z^{top} -c_p \rho Q_{rad} dz / L_v \tag{7}$$

where q^* is the saturation vapor mixing ratio, c_p is the isobaric specific heat, ρ is air density, L_v is the latent heat of vaporizaiton. The left hand side (LHS) represents the net water vapor transported upward across level z by saturated updraft and unsaturated subsidence. In steady state, this transport of vapor must be balanced by the net condensation, which is required to balance the total radiative cooling above level z (the right hand side, RHS). Since in the model the prescribed the radiative cooling is constant at $-1K\ day^{-1}$ for troposphere where temperature is larger then 250K, the change in RHS is relatively small, especially for the lower and middle troposphere. When we increase the horizontal mixing (Fig. 8), the relative humidity increases, and more clouds get detrained. The temperature through the whole troposphere also decreases, leading to a de-

creasing saturation vapor mixing ratio q^*. To satisfy the equation, the mass flux on the LHS has to increase to provide enough upward vapor transport.

4 Conclusions and Discussion

In this work, we investigated the mechanisms underlying the dependence of anvil cloud fraction on horizontal model resolution in small domain radiative-convective equilibrium (RCE) simulations. Our findings indicate that finer resolutions yield a larger anvil cloud fraction due to increased convective updrafts mass flux and enhanced mass detrainment at anvil levels, aligning with Jeevanjee and Zhou (2022) (hereafter JZ22). Further examination revealed contributing processes to the mass flux increase near the anvil level. We leveraged two distinct microphysics schemes—one a single-moment scheme, the other a double-moment Morrison scheme—to reveal that finer resolutions enhance cloud evaporation efficiency and entrainment rate, both of which are the consequence of enhanced horizontal mixing and could contribute to changes in mass flux.

In addition, we used an analytical zero-buoyancy plume model (Romps, 2014; Singh et al., 2019; Romps, 2021; Singh & Neogi, 2022) to further examine the mechanisms linking horizontal mixing to the change of mass flux. We refined the analytical plume model to derive self-consistent solutions of steady-state atmosphere profiles. This analytical model can serve as a simple, nice framework to understand general behaviors of RCE. Here, this model was employed to independently test the effects of modifying fractional entrainment rate and evaporation rate on mass flux and other atmospheric variables. Our analysis revealed that increasing the fractional entrainment rate bolsters mass flux at both cloud base and near anvil level, whereas solely augmenting the evaporation rate primarily intensifies the mass flux in the lower troposphere with minimal impact on mass flux in the upper troposphere. By increasing the fractional entrainment rate alone, we observed that the increase of updraft mass flux can be attributed to either stronger latent cooling due to cloud evaporation or weaker upper-troposphere stability. The relative importance of these two processes may depend on evaporation rate. When the specified evaporation rate is lower, environmental relative humidity is lower, and the lapse rate is more sensitive to the change of entrainment rate.

The results from analytical solution confirms that changes in the horizontal mixing can drive the resolution dependency of mass flux and cloud fraction found in the numerical simulations. One insight from our study, in comparison to JZ22, is that in certain numerical simulations and analytical scenarios, the change in upper-tropospheric mass flux is predominantly driven by changes in stability resulting from modifications in the entrainment rate. Conversely, JZ22 attributes the increase of upper-tropospheric mass flux with finer resolution solely to the change in precipitation efficiency.

We observed that atmospheric profiles like cloud fraction and relative humidity start to converge when the grid size approximates 100m. The convergence when the grid size is at the order 100m may be linked to the convergence of entrainment rate and the mixing strength. We do not have a clear theory for the dependence of entrainment rate on horizontal resolution yet. A potential explanation is that coarser resolution inadequately resolves turbulent flow and cloud entrainment, and changes in sub-grid diffusion are insufficient to offset the changes in resolved turbulence. Bryan et al. (2003) demonstrated that a Smagorinsky-like sub-grid scheme is ill-suited for a grid size on the order of 1km. An inertial subrange can only manifest when the grid size is on the order of 100m. Therefore, it is plausible that once the grid size is sufficiently refined, changes in sub-grid diffusion can effectively counterbalance changes in numerical diffusion, leading to a convergence in entrainment rate and mixing strength. An ideal sub-grid turbulence parameterization should make the entrainment strength scale insensitive even with resolution at the order of 1km. This might be one reason why Bogenschutz et al. (2023) found less sensitivity of high cloud fraction compared to this study and to JZ22.

The mechanisms we proposed is based on the radiative-convective equilibrium condition. Consequently, the resolution dependence of atmospheric profiles we observed may not persist when large-scale forcing overwhelms local convective adjustment or when a simulation has not reached an equilibrium state. This likely accounts for why Khairoutdinov et al. (2009) did not find the resolution dependence of cloud fraction with finer grid size in their 24-hour simulations with observed large-scale thermodynamic forcing.

Our study has implications to global storm-resolving simulations. Based on the convergence behavior in our small-domain simulations, the properties of cloud and convection in global storm-resolving simulations may start to converge when the horizontal resolution reaches the order of 100m. The exact resolution sensitivity can be model dependence. Also, it is not clear whether the same resolution dependence we learned in small-domain simulation—increasing resolution leading to more convective updrafts and cloud fraction—can be directly applied to the tropics in global storm-resolving simulations. The influence of horizontal resolution on cloud fraction or mass flux profiles could vary or even reverse if changing grid size changes the degree of large-scale aggregation of deep convection (e.g., Becker et al., 2017). Future research could focus on investigating these potential differences to better understand the uncertainties and biases inherent in global storm-resolving simulations.

5 Open Research

The atmosphere model used to run the simulations is the System for Atmospheric Modeling (Khairoutdinov & Randall, 2003) and is available at `http://rossby.msrc.sunysb.edu/~marat/SAM.html` (version 6.10.6, Khairoutdinov, 2023). The figures in this manuscripts, created by Python version 3.9, can be reproduced using the codes and data stored at `https://doi.org/10.5281/zenodo.8397768` (Hu et al., 2023).

Appendix A Relationship between cloud evaporation and perimeter area ratio

In the preceding sections, we highlighted the increased perimeter area ratio of cloud mass at higher resolutions, which potentially leads to a greater exposure of the cloud mass to an unsaturated environment, thereby amplifying cloud evaporation. In this section, we derive a quantitative relationship between the cloud evaporation rate and the perimeter area ratio.

Consider a specific level with a unit thickness, where the cloud mass has a total area (A) and total perimeter (L). The clouds are advected in grid points through resolved horizontal wind with a representative speed of U_{adv}. Approximately half of the cloud boundary exhibits horizontal resolved wind pointing outwards from the cloud, while the other half features wind directed inward (Fig. A1). After a time step dt, the volume of clouds advected across the boundary amounts to $0.5LU_{adv}dt$ (represented by the yellow area in Fig. A1a). An equivalent volume of environmental air is advected into the original cloudy grids (illustrated by the orange area in Fig. A1a). Following advection, the SAM1MOM scheme performs saturation adjustment. The yellow cloud mass becomes fully mixed with the environmental air in the respective grids, subsequently evaporating. On average, since the cloud mixing ratio near cloud edges is relatively minimal, we assume complete evaporation of the yellow cloud mass. The evaporation associated with this yellow cloud mass should be proportional to the product of the volume and the cloud mixing ratio at the edge $q_{c,edge}$. Similarly, in the grids containing orange environmental air, a portion of the cloud must evaporate to bring the unsaturated orange environmental air to saturation. The evaporation amount would be the product of the volume and the saturation deficit $q^*_{v,env}(1 - RH)$, where $q^*_{v,env}$ represents the environmental saturation specific humidity and RH denotes relative humidity. The total evaporation rate associated with sat-

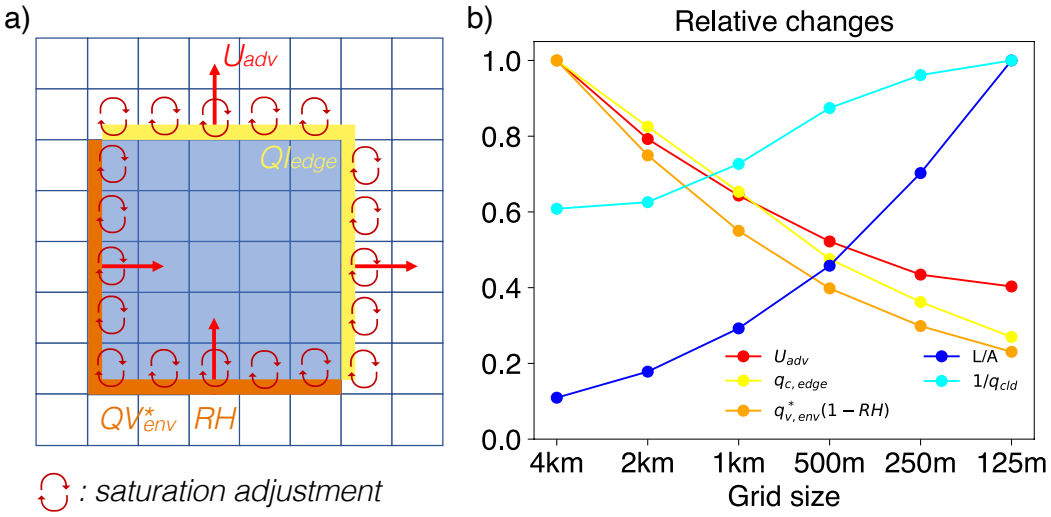

Figure A1. Panel a shows a schematic of cloud evaporation due to resolved horizontal advection and the following saturation adjustment in the SAM1MOM scheme. We set some cloud initially in the grids with blue shading and advect the cloud by horizontal wind with $U_x = U_y = U_{adv}$. $q_{c,edge}$ is the cloud mixing ratio near the cloud edge. $q^*_{v,env}$ represents the environmental saturation specific humidity, and RH denotes relative humidity in the environment near the cloud. After a small timestep dt, some cloud mass is advected into environment grids (yellow shading), and some environmental mass is advected into cloudy grids (orange shading). Circular arrows represent the saturation adjustment in each grid due to microphysics scheme. Panel b shows the relative value of different terms in Equation A4 in the SAM1MOM simulations with different resolution. Each term is standardized (divided by the maximum value across the simulations with different resolution) to have a value between 0 and 1.

uration adjustment can be expressed as:

$$Evaporation = 0.5LU_{adv}\rho[q_{c,edge} + q^*_{v,env}(1 - RH)] \tag{A1}$$

We assume all this evaporation can be counted as in the environment. We further assume the total evaporation in the environment is dominated by this numerical diffusion associated with resolved horizontal wind. This assumption likely works well for high clouds where vertical wind and sub-grid diffusion are weak, but may not work well for low clouds where vertical wind and sub-grid diffusion could be strong. Total air mass in the environment can be written as $\rho A_d f_{env}$,where A_d is domain area, f_{env} is the fraction of environment. Therefore, the latent heating rate in the environment can be written as:

$$Q_{lat,env} = 0.5LU_{adv}[q_{c,edge} + q^*_{v,env}(1 - RH)]\frac{L_v}{c_p A_d f_{env}} \tag{A2}$$

Since more clouds tend to generate more evaporation, we normalize the latent heating by the total cloud mass to get a quantity that reflect evaporation efficiency. Total cloud mass is proportional to the domain-mean cloud mixing ratio q_m, which can be further expressed as $q_m = f_{cld}q_{cld}$. f_{cld} is cloud fraction, and q_{cld} is the cloud mixing ratio averaged in cloudy grids. The normalized latent heating rate can be expressed as:

$$\frac{Q_{lat,env}}{q_m} = 0.5LU_{adv}[q_{c,edge} + q^*_{v,env}(1 - RH)]\frac{L_v}{c_p A_d f_{env} f_{cld} q_{cld}} \tag{A3}$$

Note that total cloud area can be written as $A = f_{cld}A_d$, the above equation can be rewritten as:

$$\frac{Q_{lat,env}}{q_m} = \frac{L}{A}U_{adv}\frac{q_{c,edge} + q^*_{v,env}(1 - RH)}{q_{cld}}\frac{L_v}{2c_p f_{env}} \tag{A4}$$

We define cloud boundaries as grid interfaces that separate a grid with zero cloud mixing ratio from a grid with non-zero cloud mixing ratio. Subsequently, we evaluate the average values of U_{adv}, $q_{c,edge}$, $q^*_{v,env}$, and RH at grids immediately adjacent to the boundaries, either on the inside or the outside. In Fig. A1b, we demonstrate the variation in different terms of Equation A4 as resolution becomes finer. With increased resolution, the perimeter area ratio rises, while advection velocity, cloud mixing ratio, and environmental saturation deficit decrease. The decline in near-edge cloud mixing ratio and environmental saturation deficit could be attributed to the improved representation of the transition between cloudy grids and environmental grids at finer scales. The enhanced transition at cloud boundaries in higher resolutions tends to reduce numerical diffusion and partially counterbalance the effect of the growing perimeter area ratio. The cause of the weakened advection wind and reduced in-cloud mixing ratio remains unclear and merits further investigation.

Overall, finer resolution enables better representation of turbulent cloud boundaries, which can enhance the interaction between clouds and their environment. However, finer resolution also leads to a reduction in numerical diffusion. The interplay between these two effects may be crucial in determining whether cloud evaporation efficiency converges at a specific resolution. A comprehensive understanding of these factors is essential for improving the accuracy and reliability of Earth system models.

Appendix B Refined solutions of a zero-buoyancy plume model

Here we document the details of how we solve the zero-buoyancy plume model to get self-consistent solutions about steady-state mass flux, detrainment rate, and other

atmosphere profiles. The equations we solve are:

$$\frac{\partial M_c}{\partial z} = e - d \tag{B1}$$

$$M_c + M_e = 0 \tag{B2}$$

$$\frac{\partial (M_c q^*)}{\partial z} = eq - dq^* - s_{cond} \tag{B3}$$

$$\frac{\partial (M_e q)}{\partial z} = dq^* - eq + s_{evap} \tag{B4}$$

$$\frac{\partial (M_c h^*)}{\partial z} = eh - dh^* \tag{B5}$$

$$\frac{\partial (M_e h)}{\partial z} = dh^* - eh + Q_{rad} \tag{B6}$$

$$h^* - h = L_v(q^* - q) \tag{B7}$$

$$s_{evap} = \mu d(q^* - q) \tag{B8}$$

$$\frac{\partial p}{\partial z} = -\frac{pg}{R_d T} \tag{B9}$$

Equation B1 and B2 are mass conservation equations. M_c is the mass flux of convective updrafts, and M_e is mass flux in the environment. We assume there is no large-scale advection, so the net mass flux in updrafts and in environment is 0. e is mass entrainment, and d is mass detrainment. Fractional entrainment rate ϵ and fractional detrainment rate δ are defined as:

$$\epsilon = e/M_c \tag{B10}$$

$$\delta = d/M_c \tag{B11}$$

Equation B3 and B4 describes the water vapor conservation in updraft plume and in environment separately. q is the water vapor mixing ratio in the environment. q^* is the saturation vapor mixing ratio in the updraft plume, which is simply a function of temperature and pressure:

$$q^* = 0.622 p_v^*/p = 0.622 \frac{p_0}{p} e^{-\frac{L_v}{R_v T}} \tag{B12}$$

where $p_v^* = p_0 exp(-L_v/(R_v T))$ is the saturation vapor pressure, L_v=2.51e6 J kg^{-1} is the latent heat of condensation, R_v= 461 J $kg^{-1}K^{-1}$ is gas constant for water vapor, p_0=2.69e11 Pa is a constant.

Equation B5 and B6 describes the conservation of moist static energy in updraft plume and in environment. $h = c_p T + gz + L_v q$ is the moist static energy in the environment, and $h^* = c_p T + gz + L_v q^*$ is the saturation moist static energy in the updraft plume. We specify radiative heating rate to be simply a function of temperature,

$$Q_{rad}/(c_p \rho) = \begin{cases} Q_0, & \text{if } T > 250K \\ Q_0(0.5 + 0.5cos(\pi(250 - T)/(250 - 200)), & \text{if } 250K > T > 200K \\ 0, & \text{if } T < 200K \end{cases} \tag{B13}$$

where $Q_0 = -1 K day^{-1}$. Radiative heating rate is constantly $-1 K day^{-1}$ in lower and middle troposphere and gradually decays to 0 from T=250K to T=200K. $\rho = p/R_d T$ is the air density.

Equation B7 implies the zero-buoyancy assumption that the temperature in updrafts is the same as the temperature in the environment at the same height. Equation B8 is the parameterization of cloud evaporation in the environment, following the definition in the Singh and Neogi (2022). μ is a unitless parameter which controls the speed of cloud evaporation. We assume cloud evaporation happens at the level where cloud is

condensed, and we assume there is no evaporation of precipitation. Equation B9 is the hydrostatic balance, and $R_d = 287J\,kg^{-1}K^{-1}$ is the gas constant for dry air.

For Equation B1 to B9, there are 9 equations but 11 unknown variables: M_c, M_e, ϵ, δ, q^*, q, h, s_{cond}, s_{evap}, μ, and p. We have excluded h^* and Q_{rad} from unknown variables since they can be expressed using h^* and p through Equation B12 and B13. We take ϵ and μ to be the free parameters that we can specify, and the rest of the equations is just enough to get self-consistent solution. If one further specifies δ, then there will be more equations then unknown variables, in which case there cannot be self-consistent solution. Next, we will describe how we solve these equations as an ODE problem and express the equations as $\frac{\partial}{\partial z}(M_c, p, q, T) = F(M_c, p, q, T)$.

Replacing Equation B1 into Equation B3 to B7, we can get:

$$M_c \frac{\partial q^*}{\partial z} = -\epsilon(1 - RH)M_c q^* - s_{cond} \tag{B14}$$

$$M_e \frac{\partial q}{\partial z} = \delta(1 + \mu)(1 - RH)M_c q^* \tag{B15}$$

$$M_c \frac{\partial h^*}{\partial z} = -\epsilon L_v(1 - RH)M_c q^* \tag{B16}$$

$$M_e \frac{\partial h}{\partial z} = \delta L_v(1 - RH)M_c q^* + Q_{rad} \tag{B17}$$

$RH = q/q^*$ is the relative humidity in the environment.

Equation B1 can be rewritten as:

$$\frac{\partial M_c}{\partial z} = M_c(\epsilon - \delta) \tag{B18}$$

Using Equation B2 and B15, we get:

$$\frac{\partial q}{\partial z} = -\delta(1 + \mu)(1 - RH)q^* \tag{B19}$$

Equation B16 can be used to express the temperature lapse rate $\Gamma = -\frac{\partial T}{\partial z}$. From the definition of h^*, we have:

$$\frac{\partial h^*}{\partial z} = -c_p\Gamma + g + L_v \frac{\partial q^*}{\partial z} \tag{B20}$$

Using Equation B9 and B12 and defining $\gamma = -(1/q^*)\frac{\partial q^*}{\partial z}$, we can get:

$$\gamma = \frac{L_v\Gamma}{R_v T^2} - \frac{g}{R_d T} \tag{B21}$$

Replacing Equation B20 and B21 into Equation B16, we can get:

$$\frac{\partial T}{\partial z} = \frac{1}{c_p + q^* L_v^2/(R_v T^2)}[-g(1 + \frac{L_v q^*}{R_d T}) - \epsilon L_v(1 - RH)q^*] \tag{B22}$$

When we sum Equation B3 and B4, sum Equation B5 and B6, and use Equation B2 and B7, we can get the energy balance equation:

$$Q_{rad} = L_v(s_{cond} - s_{evap}) \tag{B23}$$

Replacing Equation B8 and B14 into Equation B23, we can get the expression of M_c or δ:

$$M_c = -\frac{Q_{rad}/(L_v q^*)}{\gamma - (\epsilon + \mu\delta)(1 - RH)} \tag{B24}$$

$$\delta = -\frac{\epsilon}{\mu} + \frac{\gamma}{\mu(1 - RH)} + \frac{Q_{rad}}{\mu(1 - RH)q^* L_v M_c} \tag{B25}$$

Now with Equation B9, B18, B19, B22, and B25, we have the closed form expression for our ODE problem:

$$\frac{\partial}{\partial z}(M_c, p, q, T) = F(M_c, p, q, T) \tag{B26}$$

where the right hand side only depends on M_c, p, q, and T. Given boundary conditions at cloud base (we use z=500m), Equation B26 can integrate upwards and get the full atmosphere profiles.

For boundary conditions, we specify a surface temperature of 303K and surface pressure of 10^5 Pa. We assume dry adiabatic lapse rate of $g/c_p = 9.8Kkm^{-1}$ below cloud base, and we can use Equation B9 to integrate pressure p from the surface to cloud base. For environmental water vapor mixing ratio q at cloud base, we do not have a solid constrain. If one assumes $\frac{\partial q}{\partial z} \approx RH\frac{\partial q^*}{\partial z}$ (the vertical gradient of RH is much smaller than the vertical gradient of q^*), Equation B15 can reduce to:

$$RH = \frac{\delta(1+\mu)}{\delta(1+\mu)+\gamma} \tag{B27}$$

We determine our cloud base q using Equation B27, and the value of δ in Equation B27 is taken from the ϵ. In this way, we implicitly assumes that increasing ϵ or μ can have a moistening effect at the cloud base, which intuitively makes sense. We will show later the sensitivity of solution to the value of cloud base q.

For M_c, we do not have a direct cloud base constrain. However, we assume our solution is in radiative-convective equilibrium (RCE), which says radiative cooling must be balanced by latent heat release at all the levels. The RCE condition requires that M_c reaches 0 exactly at the level where the radiative cooling rate becomes 0, i.e., at T=200K (Equation B13). If cloud base M_c is too large, M_c will still be positive where T=200K. If cloud base M_c is too small, M_c will go to 0 before radiative cooling decays to 0. We can have a random initial guess of cloud base M_c and change our guess based on this RCE condition. Once we find lower and upper bounds of the cloud base M_c, we use binary search to iteratively guess between the bounds and narrow the bounds until we find the M_c that satisfies the RCE condition.

In Fig. B1 we test the sensitivity of the atmospheric profiles to the cloud base water vapor mixing ratio (or equivalently RH). We change the cloud base RH from 70% to 90%. Except temperature profile, the influence of cloud base RH on other variables is primarily within the lower 5km and does not have a big impact to the upper troposphere. The temperature becomes warmer through the whole troposphere with moister cloud base environment. For cloud base mass flux, it strongly depends on the RH based on Equation 5 in the main text. The way we determine the cloud base RH using Equation B27 will implicitly lead to the sensitivity that cloud base mass flux increases when ϵ or μ increase. Since our main focus in this paper is the upper troposphere mass flux, the uncertainty in how we determine the cloud base RH will likely not change our results. We also tested fixing the relative humidity at the cloud base. The sensitivities regarding to mixing strength and evaporation rate remain qualitatively the same. In future research, it would be beneficial to integrate considerations of energy and water conservation in the subcloud layer, along with surface flux parameterization, to automatically determine the cloud base relative humidity.

In Fig. B2 we test the sensitivity to different sea surface temperature. We can see that the whole troposphere becomes higher with the profiles of most quantities shifting upwards. The peak value of mass flux near the anvil level decreases with warmer surface temperature, which will indicate a weaker mass detrainment and likely a decrease of anvil cloud fraction (if lifetime is assumed to be unchanged with surface warming). The decrease of upper troposphere mass flux is consistent with the stability iris effect proposed in (Bony et al., 2016).

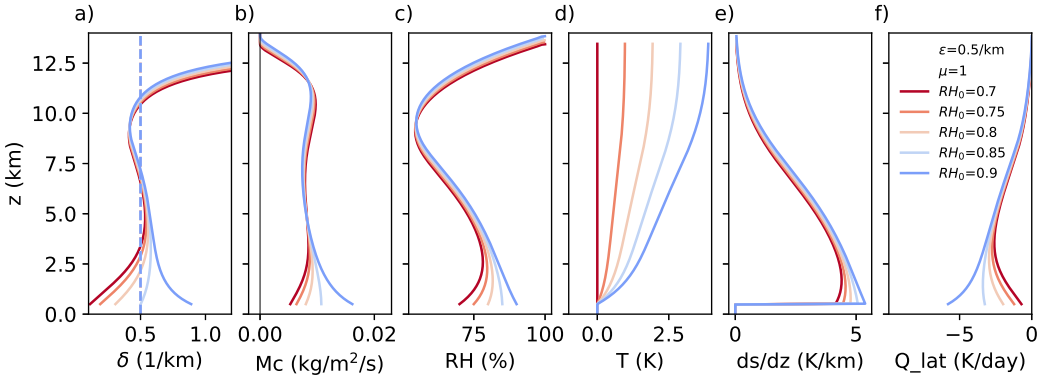

Figure B1. Atmosphere profiles in the zero-buoyancy plume model with varying cloud-base relative humidity (blue color represents more moist environment), entrainment rate $\epsilon = 0.5km^{-1}$, and cloud evaporation parameter $\mu = 1$. The variables shown are detrainment rate (a), updraft mass flux (b), relative humidity (c), temperature (d), vertical gradient of dry static energy (e), and latent heating rate due to cloud evaporation in the environment (f). Dashed lines in panel a are the profiles of prescribed entrainment rate. The temperature in panel d is shown as deviation to one of the simulations, which is denoted by the red line with zero deviation.

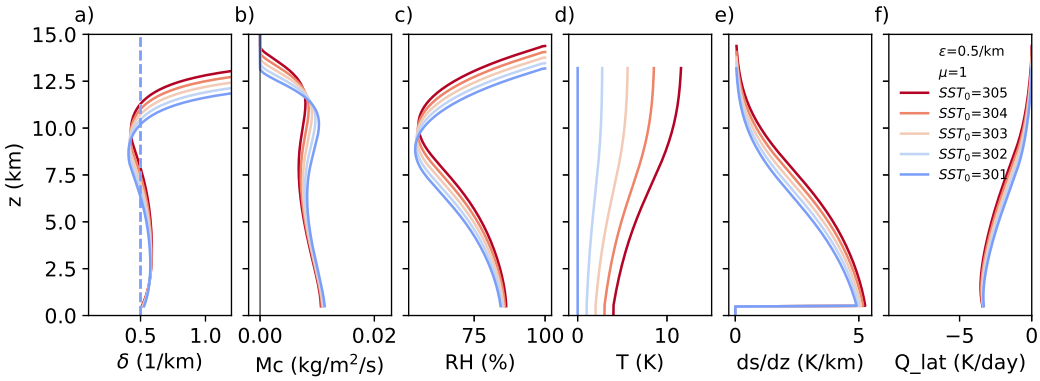

Figure B2. Similar to Fig. B1 but with sea surface temperature (blue color represents colder surface temperature), entrainment rate $\epsilon = 0.5km^{-1}$, and cloud evaporation parameter $\mu = 1$.

Acknowledgments

We thank Marat Khairoutdinov for making the SAM model available. ZH thanks Peter Blossey, Blaž Gasparini, Chris Bretherton, and Andrea Jenney for discussion/comments on this work. ZH and ZK acknowledge the funding from NSF Grant 1743753 and from the Office of Biological and Environmental Research of the U.S. DOE under grant DE-SC0022887 as part of the ASR Program. ZH acknowledges Grant DGE1745303 from NSF Graduate Research Fellowships Program.

References

Becker, T., Stevens, B., & Hohenegger, C. (2017). Imprint of the convective parameterization and sea-surface temperature on large-scale convective self-aggregation. *Journal of Advances in Modeling Earth Systems*, *9*(2), 1488–1505.

Beydoun, H., Caldwell, P. M., Hannah, W. M., & Donahue, A. S. (2021). Dissecting anvil cloud response to sea surface warming. *Geophysical Research Letters*, *48*(15), e2021GL094049.

Bogenschutz, P. A., Eldred, C., & Caldwell, P. M. (2023). Horizontal resolution sensitivity of the simple convection-permitting e3sm atmosphere model in a doubly-periodic configuration. *Journal of Advances in Modeling Earth Systems*, *15*(7), e2022MS003466. Retrieved from `https://agupubs.onlinelibrary.wiley.com/doi/abs/10.1029/2022MS003466` (e2022MS003466 2022MS003466) doi: https://doi.org/10.1029/2022MS003466

Bony, S., Stevens, B., Coppin, D., Becker, T., Reed, K. A., Voigt, A., & Medeiros, B. (2016). Thermodynamic control of anvil cloud amount. *Proceedings of the National Academy of Sciences*, *113*(32), 8927–8932.

Bony, S., Stevens, B., Frierson, D. M., Jakob, C., Kageyama, M., Pincus, R., ... others (2015). Clouds, circulation and climate sensitivity. *Nature Geoscience*, *8*(4), 261–268.

Bretherton, C. S., McCaa, J. R., & Grenier, H. (2004). A new parameterization for shallow cumulus convection and its application to marine subtropical cloud-topped boundary layers. part i: Description and 1d results. *Monthly weather review*, *132*(4), 864–882.

Bryan, G. H., Wyngaard, J. C., & Fritsch, J. M. (2003). Resolution requirements for the simulation of deep moist convection. *Monthly Weather Review*, *131*(10), 2394–2416.

Hartmann, D. L., Gasparini, B., Berry, S. E., & Blossey, P. N. (2018). The life cycle and net radiative effect of tropical anvil clouds. *Journal of Advances in Modeling Earth Systems*, *10*(12), 3012–3029.

Hohenegger, C., Kornblueh, L., Klocke, D., Becker, T., Cioni, G., Engels, J. F., ... Stevens, B. (2020). Climate statistics in global simulations of the atmosphere, from 80 to 2.5 km grid spacing. *Journal of the Meteorological Society of Japan. Ser. II*, *98*(1), 73–91.

Hu, Z., Jeevanjee, N., & Kuang, Z. (2023). From grid to cloud: Understanding the impact of grid size on simulated anvil clouds and atmospheric profiles [software].
doi: https://doi.org/10.5281/zenodo.8397768

Hu, Z., Lamraoui, F., & Kuang, Z. (2021). Influence of upper-troposphere stratification and cloud–radiation interaction on convective overshoots in the tropical tropopause layer. *Journal of the Atmospheric Sciences*, *78*(8), 2493–2509.

Iacono, M. J., Delamere, J. S., Mlawer, E. J., Shephard, M. W., Clough, S. A., & Collins, W. D. (2008). Radiative forcing by long-lived greenhouse gases: Calculations with the aer radiative transfer models. *Journal of Geophysical Research: Atmospheres*, *113*(D13).

Jeevanjee, N. (2017). Vertical velocity in the gray zone. *Journal of Advances in Modeling Earth Systems*, *9*(6), 2304–2316.

Jeevanjee, N. (2022). Three rules for the decrease of tropical convection with global warming. *Journal of Advances in Modeling Earth Systems*, *14*(11), e2022MS003285.

Jeevanjee, N., & Zhou, L. (2022). On the resolution-dependence of anvil cloud fraction and precipitation efficiency in radiative-convective equilibrium. *Journal of Advances in Modeling Earth Systems*, *14*(3), e2021MS002759.

Khairoutdinov, M. (2023). System for atmospheric modeling [software]. Retrieved from `http://rossby.msrc.sunysb.edu/~marat/SAM/`

Khairoutdinov, M., Krueger, S. K., Moeng, C.-H., Bogenschutz, P. A., & Randall, D. A. (2009). Large-eddy simulation of maritime deep tropical convection. *Journal of Advances in Modeling Earth Systems*, *1*(4).

Khairoutdinov, M., & Randall, D. A. (2003). Cloud resolving modeling of the arm summer 1997 iop: Model formulation, results, uncertainties, and sensitivities. *Journal of the Atmospheric Sciences*, *60*(4), 607–625.

Kuang, Z., & Bretherton, C. S. (2006). A mass-flux scheme view of a high-resolution simulation of a transition from shallow to deep cumulus convection. *Journal of the Atmospheric Sciences*, *63*(7), 1895–1909.

Miyamoto, Y., Kajikawa, Y., Yoshida, R., Yamaura, T., Yashiro, H., & Tomita, H. (2013). Deep moist atmospheric convection in a subkilometer global simulation. *Geophysical Research Letters*, *40*(18), 4922–4926.

Morrison, H., Curry, J., & Khvorostyanov, V. (2005). A new double-moment microphysics parameterization for application in cloud and climate models. part i: Description. *Journal of the atmospheric sciences*, *62*(6), 1665–1677.

Powell, S. W., Houze, R. A., Kumar, A., & McFarlane, S. A. (2012). Comparison of simulated and observed continental tropical anvil clouds and their radiative heating profiles. *Journal of the Atmospheric Sciences*, *69*(9), 2662–2681.

Romps, D. M. (2014). An analytical model for tropical relative humidity. *Journal of Climate*, *27*(19), 7432–7449.

Romps, D. M. (2021). Ascending columns, wtg, and convective aggregation. *Journal of the Atmospheric Sciences*, *78*(2), 497–508.

Satoh, M., Stevens, B., Judt, F., Khairoutdinov, M., Lin, S.-J., Putman, W. M., & Düben, P. (2019). Global cloud-resolving models. *Current Climate Change Reports*, *5*, 172–184.

Seeley, J. T., Jeevanjee, N., Langhans, W., & Romps, D. M. (2019). Formation of tropical anvil clouds by slow evaporation. *Geophysical Research Letters*, *46*(1), 492–501.

Sherwood, S., Webb, M. J., Annan, J. D., Armour, K. C., Forster, P. M., Hargreaves, J. C., ... others (2020). An assessment of earth's climate sensitivity using multiple lines of evidence. *Reviews of Geophysics*, *58*(4), e2019RG000678.

Siebesma, A., & Jonker, H. (2000). Anomalous scaling of cumulus cloud boundaries. *Physical review letters*, *85*(1), 214.

Singh, M. S., & Neogi, S. (2022). On the interaction between moist convection and large-scale ascent in the tropics. *Journal of Climate*, *35*(14), 4417–4435.

Singh, M. S., & O'Gorman, P. A. (2013). Influence of entrainment on the thermal stratification in simulations of radiative-convective equilibrium. *Geophysical Research Letters*, *40*(16), 4398–4403.

Singh, M. S., Warren, R. A., & Jakob, C. (2019). A steady-state model for the relationship between humidity, instability, and precipitation in the tropics. *Journal of Advances in Modeling Earth Systems*, *11*(12), 3973–3994.

Stevens, B., Satoh, M., Auger, L., Biercamp, J., Bretherton, C. S., Chen, X., ... others (2019). Dyamond: the dynamics of the atmospheric general circulation modeled on non-hydrostatic domains. *Progress in Earth and Planetary Science*, *6*(1), 1–17.

902 Wing, A. A., Stauffer, C. L., Becker, T., Reed, K. A., Ahn, M.-S., Arnold, N. P.,
903 ... others (2020). Clouds and convective self-aggregation in a multimodel
904 ensemble of radiative-convective equilibrium simulations. *Journal of Advances*
905 *in Modeling Earth Systems*, *12*(9), e2020MS002138.
906 Zelinka, M. D., Myers, T. A., McCoy, D. T., Po-Chedley, S., Caldwell, P. M., Ceppi,
907 P., ... Taylor, K. E. (2020). Causes of higher climate sensitivity in cmip6
908 models. *Geophysical Research Letters*, *47*(1), e2019GL085782.